

Effective Locomotion at Multiple Stride Frequencies Using Proprioceptive Feedback on a Legged Microrobot

Neel Doshi^{1,2,‡}, Kaushik Jayaram^{1,2,‡}, Samantha Castellanos^{1,2}, Scott Kuindersma¹ and Robert J. Wood^{1,2}

¹ John A. Paulson School of Engineering and Applied Sciences, Harvard University, Cambridge, MA, USA

² Wyss Institute for Biologically Inspired Engineering, Cambridge, MA, USA

E-mail: ndoshi, kjayaram @seas.harvard.edu

Abstract. Limitations in actuation, sensing, and computation have forced small legged robots to rely on carefully tuned, mechanically mediated leg trajectories for effective locomotion. Recent advances in manufacturing, however, have enabled the development of small legged robots capable of operation at multiple stride frequencies using multi-degree-of-freedom leg trajectories. Proprioceptive sensing and control is key to extending the capabilities of these robots to a broad range of operating conditions. In this work, we leverage concomitant sensing for piezoelectric actuation to develop a computationally efficient framework for estimation and control of leg trajectories on a quadrupedal microrobot. We demonstrate accurate position estimation ($<16\%$ root-mean-square error) and control ($<16\%$ root-mean-square tracking error) during locomotion across a wide range of stride frequencies (10–50 Hz). This capability enables the exploration of two parametric leg trajectories designed to reduce leg slip and increase locomotion performance (e.g., speed, cost-of-transport, etc.). Using this approach, we demonstrate high performance locomotion at stride frequencies of (10–30 Hz) where the robot’s natural dynamics result in poor open-loop locomotion. Furthermore, we identify regions of highly dynamic locomotion, low cost-of-transport (3.33), and minimal leg slippage ($<10\%$).

Keywords: self-sensing, linear-quadratic-gaussian control, legged microrobots, piezoelectric actuation, robust locomotion

Submitted to: *Bioinspir. Biomim.*

‡ These authors contributed equally

1. Introduction

Terrestrial animals use a variety of complex leg trajectories to navigate natural terrains [1]. The choice of leg trajectory is often determined by a combination of morphological factors including posture [2], hip and leg kinematics [3], ankle and foot designs [4], and actuation capabilities (e.g., muscle mechanics [5, 6]). In addition, animals also modify their leg trajectories to meet performance requirements such as speed [7], stability [8, 9], and economy [10], as well as to adapt to external factors such as terrain type [11, 12] and surface properties [13, 14].

Inspired by their biological counterparts, large (body length (BL) ~ 100 cm) bipedal [15, 16] and quadrupedal [17, 18, 19, 20] robots typically have two or more actuated degrees-of-freedom (DOF) per leg to enable complex leg trajectories. This dexterity is leveraged in a variety of control schemes to adapt to different environments and performance requirements. For example, optimization algorithms have been used to command leg trajectories to enable stable, dynamic locomotion on the Atlas bipedal [21] and HyQ quadrupedal [19] robots. Furthermore, the MIT Cheetah [18] relies on a hierarchical control scheme where the low-level controllers alter leg trajectories to directly modulate ground reaction forces.

However, as the robot's size decreases, manufacturing and material limitations constrain the number of actuators and sensors. Consequently, a majority of medium (BL ~ 10 cm) [22] and small (BL ~ 1 cm) [23, 24, 25] legged robots have at most single DOF legs driven by a hip actuator. In such systems, leg trajectory is dictated by the transmission design, and these robots often rely on tuned passive dynamics to achieve efficient locomotion [26, 27]. Nevertheless, careful mechanical design allows these robots to demonstrate impressive capabilities, including high-speed running [28], jumping [29], climbing [30, 31], horizontal to vertical transitions [12], and confined space locomotion [14].

Recent work has also focused on developing whole-body locomotion control schemes for the autonomous operation of these small legged robots. These include controllers designed using stochastic kinematic models on the octopedal OctoRoACH [32] and using deep reinforcement learning on the hexapedal VelociRoACH [33] robots. However, these robots do not have the mechanical dexterity to actively vary the shape of the their leg trajectory and instead rely on mechanical

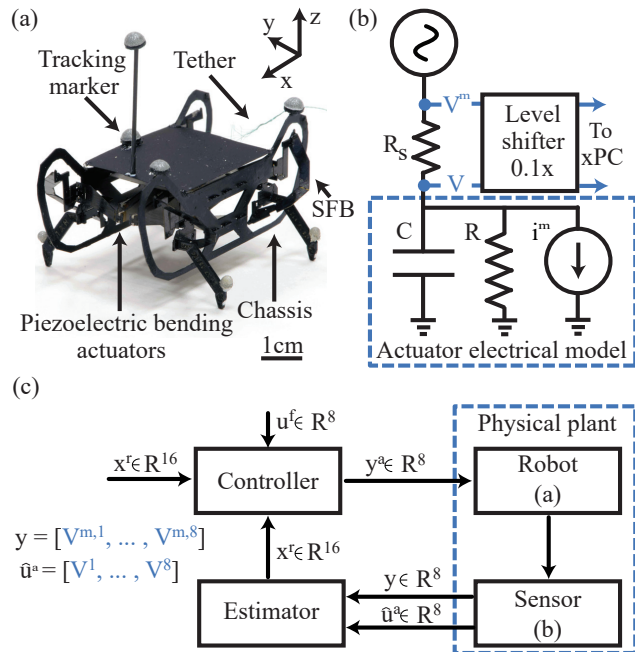


Figure 1. (a) Image of HAMR with body-fixed axes shown, and tracking markers and components labeled. (b) Schematic of a lumped parameter electrical model of a single actuator and associated piezoelectric encoder measurement circuit [38]. (c) A block diagram of the proposed sensing and control architecture. Here x^r is the reference actuator position and velocity, \hat{x}^a is estimated actuator position and velocity, u^f is the feed-forward actuator voltage, u^a is the control voltage, and \hat{u}^a and y are the sensor measurements. The design of the estimator and controller are discussed in Secs. 3 and 4, respectively.

tuning and inter-leg timing (i.e., gait) to achieve effective locomotion at a specific operating frequency.

In contrast, the Harvard Ambulatory MicroRobot (HAMR, Fig. 1a) is able to independently control the fore-aft and vertical position of each leg using high-bandwidth piezoelectric bending actuators. This dexterity enables control over both the shape of individual leg trajectories and gait. Furthermore, HAMR is unique among legged robots in its ability to operate at a wide range of stride frequencies. Despite HAMR's dexterity, however, a lack of sensing and control has limited its operation to using feed-forward sinusoidal voltage inputs resulting in elliptical leg trajectories [34, 35]. Though this approach has previously enabled rapid locomotion [36], high-performance operation (e.g., high speed, low cost-of-transport, etc.) has been limited to a narrow range of stride frequencies [37].

In this work, we leverage concomitant sensing for piezoelectric actuation (Fig. 1b, [38]) to develop a computationally inexpensive estimator and controller (Fig. 1c) for tracking leg trajectories on a microrobot. The robot and concomitant sensors and discussed in Sec. 2. We then describe the development of the estimator (Sec. 3) and controller (Sec. 4) and include an important simplification, treating of ground contact as a perturbation. We leverage this capability to track two heuristically designed parametric leg trajectories that modulate intra-leg timing, energy, and stiffness (Sec. 5). We experimentally evaluate these trajectories (Sec. 6), and demonstrate that our framework enables accurate estimation (Sec. 7.1) and tracking (Sec. 7.2) for our operating conditions (10-50 Hz). Furthermore, we find that these trajectories allow the robot to maintain locomotion performance in the body dynamics frequency regime by reducing leg slip, improving cost-of-transport (COT), and favorably utilizing body dynamics (Sec. 8). We generalize these results across the range of operating stride frequencies in Sec. 9, and the discuss implications of this work and potential future extensions in Sec. 10.

2. Platform Overview

This section describes the relevant properties of the microrobot (Sec. 2.1 and the concomitant sensors (Sec. 2.2).

2.1. Robot Description

HAMR (Fig. 1a) is a 4.5 cm long, 1.4 g quadrupedal microrobot with eight independently actuated DOFs [39]. Each leg has two DOFs that are driven by optimal energy density piezoelectric bending actuators [40]. These actuators are controlled with AC voltage signals using a simultaneous drive configuration described in [41]. A spherical-five-bar (SFB) transmission connects the two actuators to a single leg in a nominally decoupled manner: the swing actuator controls the leg’s fore-aft position, and the lift actuator controls the leg’s vertical position. A minimal-coordinate representation of the pseudo-rigid body dynamics of this robot has a configuration vector $q = [q^{fb}, q^a]^T \in \mathbb{R}^{14}$ and takes the AC voltages signals $u^a \in \mathbb{R}^8$ as inputs. The configuration vector consists of the floating base position and orientation ($q^{fb} \in \mathbb{R}^6$), and the tip deflections of the eight actuators ($q^a \in \mathbb{R}^8$). An alternative minimal-coordinate representation occasionally used in this work is $q^{alt} = [q^{fb}, q^l]^T \in \mathbb{R}^{14}$. Here $q^l \in \mathbb{R}^8$ is the vector of the four legs’ fore-aft (l^x) and vertical (l^z) positions, and it is related to q^a by a one-to-one kinematic transformation.

2.2. Sensor Design and Dynamics

Eight off-board piezoelectric encoders provide measurements of actuator tip-velocities ($\dot{q}^a \in \mathbb{R}^8$) [38]. Though these sensors are currently off-board, an on-board implementation is straightforward as the components are both light (< 10 mg) and small (< 5 mm²). Previous work has shown that the tip-velocity of a i -th actuator (\dot{q}_i^a) is α times the *mechanical current* (i^m) produced by that actuator’s motion; that is,

$$\dot{q}_i^a = \alpha i^m. \quad (1)$$

Each encoder (Fig. 1b) measures the mechanical current by applying Kirchoff’s law to the measurement circuit in series with a lumped-parameter electrical model of an actuator:

$$i^m = \frac{V^m - V}{R_s} - \beta C \dot{V} - \frac{V}{R}. \quad (2)$$

The first term on the RHS of Eqn. (2) is the total current drawn by an actuator computed from measurements of the voltage before (V^m) and after (V) a shunt resistor ($R_s = 75$ k Ω). The actuator is modeled as a capacitor (C), resistor (R), and current source (i^m) in parallel. The voltage and frequency dependent values of R and C have been computed for the range inputs in [38]. Finally, β is a blocking factor which accounts for imperfect measurements of C , and is set to 1.57 as in [38].

3. Estimator Design

We develop a proprioceptive estimator for leg position and velocity ($x^a = [q^a, \dot{q}^a]^T \in \mathbb{R}^{16}$). These estimates are used with a feedback controller to command a variety of leg trajectories for improved locomotion. To simplify the measurement model, we leverage the one-to-one map between leg and actuator position to work in the actuator frame. In theory, the actuator velocity measurements from Eqn. (1) can be integrated to estimate actuator positions (q^a). However, errors in the estimate of \dot{q}^a lead to a linear drift in the estimate of q^a . This drift is often mitigated by incorporating additional information from different sensors, a model of the system dynamics, or both.

For our application, size and payload constraints make it difficult to incorporate additional sensors on the microrobot. Computational constraints also make it impractical to use high-fidelity process models that resolve the discontinuous mechanics of ground contact online [42]. As such, we ignore contact to develop an infinite-horizon Kalman filter that combines a linear approximation of the pseudo-rigid body dynamic model developed in [43] with the measurement model described in Eqns. (1-2). This filter averages a

drifting position measurement that registers ground contact with a zero-drift position prediction that ignores contact, with the primary advantage that all quantities used in the update rule are pre-computed.

3.1. Process Model

Given that we are ignoring ground contact, a single transmission can be modeled in isolation. The minimal-coordinate dynamics of each SFB transmission in the actuator-frame (Note S1) can be written in the standard form as:

$$x_{k+1}^p = f(x_k^p, u_k^p), \quad (3)$$

where k is the time-step, $x_k^p = [q_k^s, \dot{q}_k^s, q_k^l, \dot{q}_k^l]^T \in \mathbb{R}^4$ is the position and velocity of the swing and lift actuators, and $u_k^p = [V_k^s, V_k^l]^T \in \mathbb{R}^2$ are the actuator drive voltages. Instead of calculating the linear approximation of $f(x_k^p, u_k^p)$ about a fixed point (x_0^p, u_0^p) , we use subspace system identification techniques [44] to determine a discrete-time second-order (four-state) linear system that minimizes the prediction error for the range of expected actuator deflections (± 0.15 mm) and stride frequencies (10–50 Hz). While the accuracy of a local linear approximation decreases away from the fixed point, the identified model is accurate in an average sense across the range of expected operating conditions. The identification of this linear model is described in Note S2, and the resulting discrete-time linear system has the form

$$x_{k+1}^p = A^p x_k^p + B^p (u_k^p - u_0^p) + w_k^p, \quad (4)$$

with $A^p \in \mathbb{R}^{4 \times 4}$ and $B^p \in \mathbb{R}^{4 \times 2}$. The signal $w_k^p \in \mathbb{R}^4$ is zero-mean process noise with covariance W^p . Finally, note that x^p and u^p are subsets of x^a and u^a corresponding to the appropriate transmission, and the identical procedure is carried out to develop a process model for each transmission.

3.2. Measurement Model

Since each piezoelectric encoder measurement is independent, the sensor dynamics (Sec. 2.2) is inverted to form the measurement model for a single actuator. We start by combining Eqns. (1-2) with a finite difference approximation of \dot{V} to write a difference equation for \dot{q}_k :

$$\dot{q}_k = c_1(V_k^m - V_k) - c_2 V_k - c_3(V_k - V_{k-1}), \quad (5)$$

where $c_1 = \alpha R_s^{-1}$, $c_2 = \alpha R^{-1}$, and $c_3 = \alpha \beta C h^{-1}$. Since Eqn. (5) depends on the previous time-step, we also write a difference equation for \dot{q}_{k-1} using the same finite difference approximation for \dot{V}_{k-1} :

$$\dot{q}_{k-1} = c_1(V_{k-1}^m - V_{k-1}) - c_2 V_{k-1} - c_3(V_k - V_{k-1}). \quad (6)$$

Combining Eqns. (5) and (6) and solving for $y_k^m = [V_k^m, V_{k-1}^m] \in \mathbb{R}^2$ gives the measurement model:

$$y_k^m = H^m x_k^m + D^m u_k^m + n_k^m. \quad (7)$$

Here

$$H^m = \frac{1}{c_1} \begin{bmatrix} 0_{2 \times 1} & I_{2 \times 2} \end{bmatrix} \in \mathbb{R}^{2 \times 3}, \quad (8)$$

$$D^m = \frac{1}{c_1} \begin{bmatrix} c_1 + c_2 + c_3 & -c_3 \\ c_3 & c_1 + c_2 + c_3 \end{bmatrix} \in \mathbb{R}^{2 \times 2}, \quad (9)$$

$x_k^m = [q_k, \dot{q}_k, \dot{q}_{k-1}]^T \in \mathbb{R}^3$, and $u_k^m = [V_k, V_{k-1}] \in \mathbb{R}^2$. The signal $n_k^m \in \mathbb{R}^2$ is zero-mean measurement noise with covariance $N^m = N^H + D N^D D^T$. Note that the process and measurement states are not equal ($x^m \neq x^p$), and the following section builds an augmented state to resolve this discrepancy.

3.3. Complete Estimator

Combining the process and measurement models, we write the linearized discrete-time dynamics of a single transmission-sensor system in the following form:

$$x_{k+1} = A x_k + B u_k + w_k \quad (10)$$

$$y_k = H x_k + D u_k + n_k, \quad (11)$$

where $x_k = [(x_k^p)^T, \dot{q}_{k-1}^s, \dot{q}_{k-1}^l]^T \in \mathbb{R}^6$ is the state, $y_k = [V_k^{m,s}, V_k^{m,l}, V_{k-1}^{m,s}, V_{k-1}^{m,l}]^T \in \mathbb{R}^4$ is the measurement, $u_k = [(u_k^p)^T, (u_{k-1}^p)^T]^T \in \mathbb{R}^4$ is the input. Furthermore, $w_k \in \mathbb{R}^6$ and $n_k \in \mathbb{R}^4$ are the zero-mean process and measurement noise with covariance given by

$$W = \begin{bmatrix} W^p & 0 \\ 0 & 0 \end{bmatrix}, \quad N = \begin{bmatrix} N^m & 0 \\ 0 & N^m \end{bmatrix}, \quad (12)$$

respectively. Finally, the system matrices are given by

$$A = \begin{bmatrix} A^p & 0_{4 \times 2} \\ [e_2, e_3]^T & 0_{2 \times 2} \end{bmatrix} \in \mathbb{R}^{6 \times 6} \quad (13)$$

$$B = \begin{bmatrix} B^p & 0_{2 \times 2} \\ 0_{2 \times 2} & 0_{2 \times 2} \end{bmatrix}, \in \mathbb{R}^{6 \times 4} \quad (14)$$

$$H = \begin{bmatrix} 0 & h_{11}^m & 0_{1 \times 4} \\ 0_{1 \times 2} & h_{11}^m & 0_{1 \times 3} \\ 0_{1 \times 4} & h_{22}^m & 0 \\ 0_{1 \times 4} & 0 & h_{22}^m \end{bmatrix} \in \mathbb{R}^{4 \times 6} \quad (15)$$

$$D = \begin{bmatrix} d_{11}^m & 0 & d_{12}^m & 0 \\ 0 & d_{11}^m & 0 & d_{12}^m \\ d_{21}^m & 0 & d_{22}^m & 0 \\ 0 & d_{21}^m & 0 & d_{22}^m \end{bmatrix} \in \mathbb{R}^{4 \times 4}. \quad (16)$$

Here h_{ij}^m and d_{ij}^m are ij -th entries of H^m and D^m , respectively, and e_2 and e_3 are elementary unit vectors in \mathbb{R}^4 . Given this formulation, the infinite-horizon Kalman gain is computed off-line as $K =$

$PH(HPH^T + R)^{-1} \in \mathbb{R}^{6 \times 4}$, where P is found by solving the discrete-time algebraic Ricatti equation [45]. The current state estimate is then given by

$$\hat{x}_k = A\hat{x}_{k-1} + Bu_{k-1} + K(y_k - H(A\hat{x}_{k-1} + Bu_{k-1}) - Du_k), \quad (17)$$

where the state is initialized to $\hat{x}_0 = 0$.

This simple update rule can be carried out independently for each transmission and only requires the addition of vectors \mathbb{R}^6 and multiplication of vectors in \mathbb{R}^6 by sparse matrices in $\mathbb{R}^{6 \times 6}$. Though the filter is currently implemented off-board, it is easy to envision an efficient real-time implementation on a microcontroller.

4. Controller Design

Similar to the complete estimator, the feedback controller is also independently derived for a transmission-sensor system. A subset of estimated actuator positions and velocities (\hat{x}_k^p) is used in a feedback controller designed as a linear-quadratic-regulator (LQR). The feedback law minimizes the following cost function:

$$J = \sum_{k=0}^{\infty} (\hat{x}_k^p - x_k^0)^T Q (\hat{x}_k^p - x_k^0) + (u_k^p - u_0^p)^T R (u_k^p - u_0^p), \quad (18)$$

where $Q \succeq 0$ and $R \succ 0$ are symmetric matrices that penalize deviations from the fixed point (x_0^p, u_0^p) . We defined Q and R as diagonal matrices parameterized by three positive scalars (k_p , k_d , and k_u) that determine trade-offs between squared deviations in actuator position, velocity, and control voltage, respectively. The complete control law combines the LQR feedback rule with a feed-forward term ($u_k^f = u_0^p + u_k^t \in \mathbb{R}^2$):

$$u_k^p = u_k^f + L(x_k^r - \hat{x}_k^p). \quad (19)$$

Here $x_k^r \in \mathbb{R}^4$ is the reference state, $L = (R + B^T S B)^{-1} B^T S A \in \mathbb{R}^{2 \times 4}$ is the feedback matrix, and S is computed by solving the discrete-time algebraic Ricatti equation [45]. The resulting linear-quadratic-Gaussian (LQG) dynamical system is formulated by combining Eqn. (17) with the control law given in Eqn. (19).

Intuitively, the feed-forward term is equal to the nominal voltage (u_0^p) if the reference state is the fixed point. Furthermore, the control law in Eqn. (19) will stabilize the LQG system since Q and R are chosen to be positive-definite. In practice, the controller is used to track reference trajectories on the physical (nonlinear) legged robot, the control input (u_k^p) still acts to reduce the error, and ground reaction forces can be thought of as disturbances. We also augment

the feed-forward term with a time varying component (u_k^t) that is computed via a trajectory optimization without ground contact (Note S3). This term is similar to the nominal input for a time-varying LQR controller about a trajectory; however, the lack of ground contact modeling makes it more of a heuristic for improving the convergence rate and reducing steady-state error.

5. Trajectory Design

Using the estimation and control framework described in the previous two sections (Secs. 3 and 4), we are now able to track arbitrary leg trajectories subject to the dynamics of the transmission. We exploit this to expand on our previous work that explored the effect of gait and stride frequency on locomotion [37]. The major challenges that limited locomotion performance in our previous studies are:

- (1) High leg-slip (40 -45% ineffective stance) across all stride frequencies.
- (2) Increased body oscillations (in roll and pitch) in the body dynamics frequency range (20-40 Hz).
- (3) Departure from SLIP-dynamics [46] beyond the mechanically tuned operating point close to robot z -resonance (~ 10 Hz).
- (4) Fixed (open-loop) timing between vertical and fore-aft resulting in poor or backwards locomotion (e.g., when pronking at 10 Hz).

In this work, we postulate the following four specific hypotheses to understand the underlying mechanisms behind the challenges enumerated above.

- (H₁) Increasing the leg retraction period reduces slipping and improves locomotion performance.
- (H₂) Increasing input lift energy, especially in the body dynamics frequency range, increases detrimental body-oscillations and reduces locomotion performance.
- (H₃) Increasing effective leg stiffness allows for greater energy storage and return (SLIP-like dynamics) and improves performance at higher stride frequencies.
- (H₄) The timing between the vertical and fore-aft leg motions that results in the best performance varies as a function of stride frequency.

These hypotheses are distilled into parametric leg trajectories for the trot (Fig. 2a) and pronk (Fig. 2b) gait, respectively. Each trajectory is defined by five parameters described in Tab. 1. Here, the swing (A_S) and lift (A_L) actuator amplitudes are held constant, T controls the stride frequency, and the shape parameters S_1 and S_2 vary as described below. For both parametric trajectories, we address H_1 by maintaining a constant speed during leg retraction and

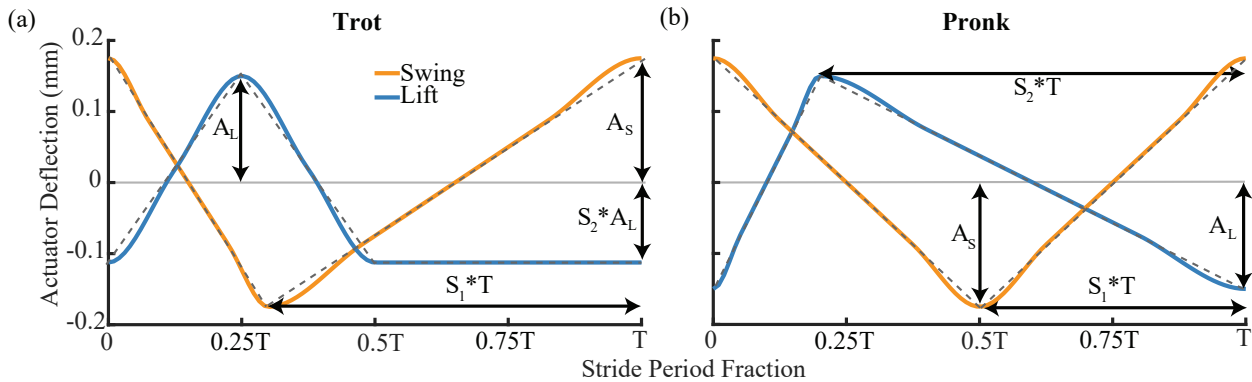


Figure 2. (a) Reference actuator positions for the swing (orange) and lift (blue) for the trot gait leg trajectory with $S_1 = 70$, and $S_2 = 75$. (b) The same for the pronk gait leg trajectory with $S_1 = 50$, and $S_2 = 80$. Note that A_S and A_L are fixed to the values given in Tab. 1, and the smooth reference trajectories (in orange and blue) are generated by fitting a cubic-spline to the non-smooth desired trajectories (grey dashed lines).

Table 1. Heuristic trajectory design parameters

Parameters	Description	Trot Gait	Pronk Gait
A_S	swing amplitude	175 μm	150 μm
A_L	lift amplitude	175 μm	150 μm
T	stride period (1/frequency)	$\in [1/50, 1/40, 1/30, 1/20, 1/10]$ ms	$\in [1/50, 1/40, 1/30, 1/20, 1/10]$
S_1	shape control one	leg retraction period (% T) $\in [50, 60, 70, 80]$	leg retraction period (% T) $\in [50, 60, 70, 80]$
S_2	shape control two	maximum leg adduction (% A_L) $\in [-75, -50, -25, 0, 25]$	leg adduction period (% T) $\in [20, 35, 50, 65, 80]$

vary the leg retraction period as a trajectory shape control parameter S_1 . For the trot gait, we also vary the maximum leg adduction via the shape parameter S_2 . This modification directly varies the net energy imparted to the lift (z) motion addressing H_2 . In addition S_2 also modulates leg stiffness (see Fig S2 and Note S3) addressing H_3 . Finally, we vary the leg adduction period as the trajectory shape control parameter S_2 for the pronk gait. This modification, coupled with S_1 from above, varies the timing between the vertical and fore-aft leg motions addressing H_4 .

Ultimately, we hypothesize (H_5) that exploring the leg trajectories described above can reveal optimized shape control parameters that enable high-performance locomotion over the entire operating range of the robot, overcoming challenges observed in our previous research [37].

6. Experimental Design, Methods and Metrics

This section first describes the calibration conducted before running experiments (Sec 6.1). We then describe the experimental procedures and apparatus for evaluating the estimator (Sec. 3) and controller (Sec. 4) performance, and for exploring the heuristic

leg trajectories (Sec. 5). Finally, we define a number of locomotion performance metrics in Sec. 6.4 that are used to quantify the effects of varying leg trajectory shape (Sec. 8).

6.1. Calibration

A calibration was performed for each robot and single-leg before conducting all experiments. The measurement noise covariances N^H and N^D were computed from mean-subtracted measurements of V^m and V , respectively, with $u^a = 0$. These means (corresponding to an initial offset) were also subtracted from subsequent measurements of V^m and V . The velocity scaling coefficients (α) from the mechanical current (mA) to tip velocity (mms^{-1}) were computed for each actuator over the range of operating frequencies. The coefficient for each actuator was set to the value that minimized the squared-error between the mechanical current (i_m , Eqn. (2)), and corresponding ground-truth leg velocity.

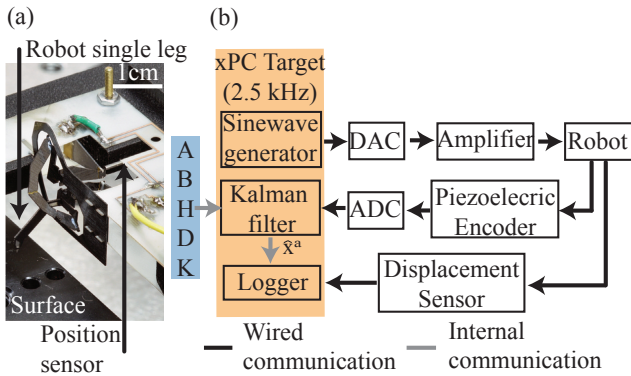


Figure 3. (a) Experimental setup with single-leg used to evaluate estimator performance, with components labeled. Ground truth is provided by a calibrated fiber-optic displacement sensor (Philtec-D21) at 2.5 kHz. (b) Communication and estimation block diagram for estimator characterization in the actuator frame with blocks implemented on the xPC target shaded in orange. Note that the Kalman updated gains (matrices A , B , H , D , and K ; shaded in blue) are pre-computed off-line.

6.2. Estimator Validation

Estimator validation was conducted on a single-leg (Fig. 3a) using the architecture shown in Fig 3b. Sinusoidal input signals were generated at 2.5 kHz using a MATLAB xPC environment (MathWorks, R2015a), and were supplied to the single-leg through a four-wire tether. The Kalman filter (Sec. 3) estimated actuator position and velocity from the voltage measurements provided by two piezoelectric encoders at 2.5 kHz. Finally, ground truth swing and lift actuator position measurements were provided by calibrated fiber-optic displacement sensors (Philtec-D21) at the same rate.

We measured estimator performance at stride frequencies of 10, 20, 30, 40, and 50 Hz both in-air (5 trials, 15 cycles each) and with ground-contact (5 trials, 15 cycles each). Ground contact was achieved by positioning a surface at the neutral position of the leg for the duration of the trial. Estimation error for a single actuator was quantified as \bar{E}_{est} , which is the N -cycle mean of the RMS error between the estimated actuator position and ground-truth measurements normalized by the peak-to-peak amplitude of the ground-truth measurements.

We also quantified estimator performance on a full-robot (10 trials, 15 cycles each) at frequencies of 10, 20, 30, 40, and 50 Hz using the locomotion arena shown in Fig. 4a to determine if the estimator could also be used to accurately predict leg positions (l^x, l^z). Once again, we used sinusoidal input signals and conducted five trials in air and five trials with the robot running on a card-stock surface. These trials were conducted using the architecture shown in Fig. 4b with the control gains set to zero. The set-up described above as expanded

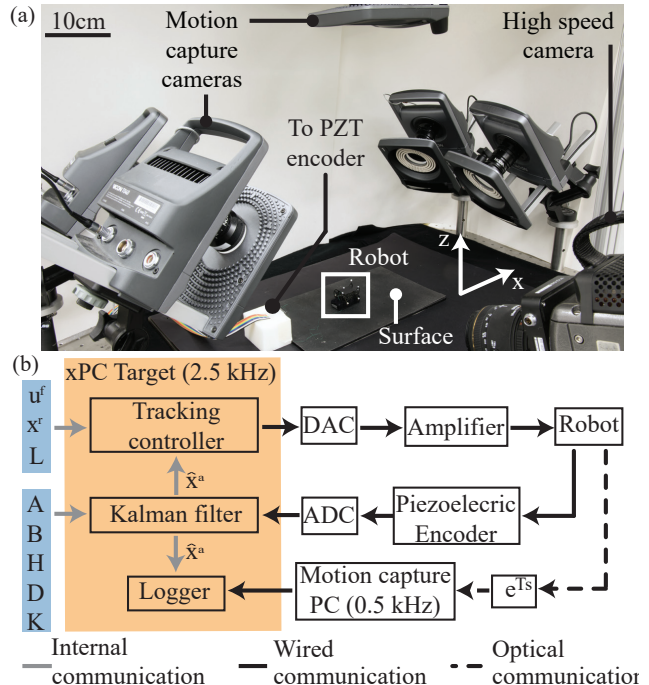


Figure 4. (a) Perspective image of the locomotion arena with components and world-fixed axes labeled. (b) Communication and control block diagram for the leg trajectory exploration trials. The Kalman filter and tracking controller run on the xPC target (shaded in orange) at 2.5 kHz. Reference actuator trajectories (x^r), the feedback control-law (L), the Kalman update (matrices A , B , H , D , and K), and the feed-forward control signals (u^{ff}) are shaded in blue and are pre-computed off-line.

to accommodate eight actuators, and five motion capture cameras (Vicon T040) tracked the position and orientation of the robot at 500 Hz with a latency of 11 ms. A custom C++ script using the Vicon SDK enabled tracking of the leg tips in the body-fixed frame. We used a model of the transmission kinematics to map the estimated actuator position to l^x and l^z , and these estimates were compared against ground truth leg position measurements provided by the motion-capture system. Performance was quantified using \bar{E}_{est} with estimated and ground-truth leg positions averaged across all four transmissions of a robot.

6.3. Closed-loop Performance Validation and Leg Trajectory Exploration

In addition to the open-loop estimator validation experiments, we performed 400 closed-loop trials to evaluate HAMR's performance when using the two classes of heuristic leg trajectories (Sec. 5). These experiments used two robots whose floating-base natural frequencies are characterized in Fig. S1 using methods described in [37]. Two hundred trials were conducted on each robot with 100 trials for each class of heuristic leg trajectory. Each subset of one

hundred trials enumerated all possible combinations of stride period (T) and shape parameters (S_1 and S_2). The 400 trials were all conducted in the locomotion arena described above. Since both robots showed similar performance, we averaged the data to compute locomotion metrics (Sec. 6.4). We evaluated the tracking performance using \bar{E}_{cont} , defined as the N -cycle mean of the RMS error between the estimated and desired actuator position measurements normalized by the peak-to-peak amplitude of the desired actuator position.

6.4. Locomotion Performance Metrics

6.4.1. Normalized per Cycle Speed (ν) This is a measure of the speed of the robot (v) during locomotion. It is defined as the ratio of speed achieved per step to the kinematic step length and is computed as

$$\nu = \frac{v}{L_s n f}, \quad (20)$$

where $L_s = 4.7$ mm is the kinematic step length, n is the number of steps per stride for a given gait ($n_{trot} = 2, n_{pronk} = 1$) and $f = \frac{1}{T}$ is the stride frequency. Intuitively, $\nu = 1$ is the expected forward speed assuming ideal kinematic locomotion, and $\nu > 1$ suggests that the robot is utilizing dynamics favorably to increase its stride length beyond the kinematic limits.

6.4.2. Step Effectiveness (σ) This is a measure of the robot leg slippage during locomotion. It is defined for each leg as one minus the ratio of leg-slip to the kinematic step length. We consider leg-slip to be the total distance a single leg travels in the direction opposite to the robot heading in the world frame. We present an average value for all four legs computed as

$$\sigma = 1 - \frac{1}{4L_s} \sum_{i=1}^4 \int_{\zeta} |v_x^i(t)| dt, \quad (21)$$

where v_x^i is the x-velocity of the i^{th} leg in the world-fixed frame, and ζ is the set of times within a step for which v_x^i is in the opposite direction as the robot heading. Intuitively, $\sigma = 1$ indicates no slipping while $\sigma = 0$ indicates continuous slipping (i.e., no locomotion of the robot).

6.4.3. Locomotion Economy (ϵ) This is a measure of the the robot's COT [47]. This is defined as the ratio of the robot's mechanical output power to the total electrical power consume and is quantified as:

$$\epsilon = \frac{mgv_x}{\sum_{i=1}^8 \frac{1}{T} \int_0^T i^m(t) V^m(t) dt}, \quad (22)$$

where $m = 1.43$ g is the mass of the robot and $g = 9.81$ ms⁻² is the acceleration due to gravity. Intuitively, lower values of ϵ indicate poor conversion of the input electrical power into mechanical output, suggesting ineffective locomotion performance.

6.5. Open-loop Control Trajectory Comparison

6.5.1. Coupled Sinusoids The RMS amplitude for each sinusoidal drive voltage was equal to the average of the RMS voltages delivered to all eight actuators during the fastest trial at a particular stride period. This control experiment did not discriminate between voltages delivered to the lift and swing DOFs and is therefore referred to as the *coupled configuration*.

6.5.2. Decoupled Sinusoids The RMS amplitude for the four lift (and four swing) actuators was equal to the average RMS voltage delivered to the lift (and swing) actuators during the fastest trial at a particular stride period, respectively. The voltages delivered to the lift and swing actuators were individually computed, and therefore, this is referred to as the *decoupled configuration*.

7. Estimator and Controller Performance

This section summarizes our results related to the quantification of estimator and controller performances.

7.1. Estimator

The performance of the estimator is shown in Fig. 5 with tracking errors for a representative trial in air and on the ground shown in supplementary Fig. S4. For the trials in air (Fig. 5a), the mean normalized estimation error in actuator position ranges from 5% at 10 Hz to 10% at 50 Hz. These numbers indicate accurate estimation in air, confirming the accuracy of both measurement and process models and serving as a baseline. Small tracking errors are likely resulting from noise in the sensor measurements and differences between the linear process model and the true non-linear dynamics. The error in leg position is higher than actuator position error and ranges from 6% at 10 Hz to 15% at 50 Hz, and we suspect this is due to inaccuracies in the modeled transmission kinematics.

Similarly, actuator position error (blue) is low when subject to approximated ground-contact. The normalized swing (Fig. 5b) and lift (Fig. 5c) actuator position errors are between 5%-10% and 8%-16%, respectively. We suspect that the lift position errors are higher because the process model does not capture the effect of (1) perturbations from ground contact

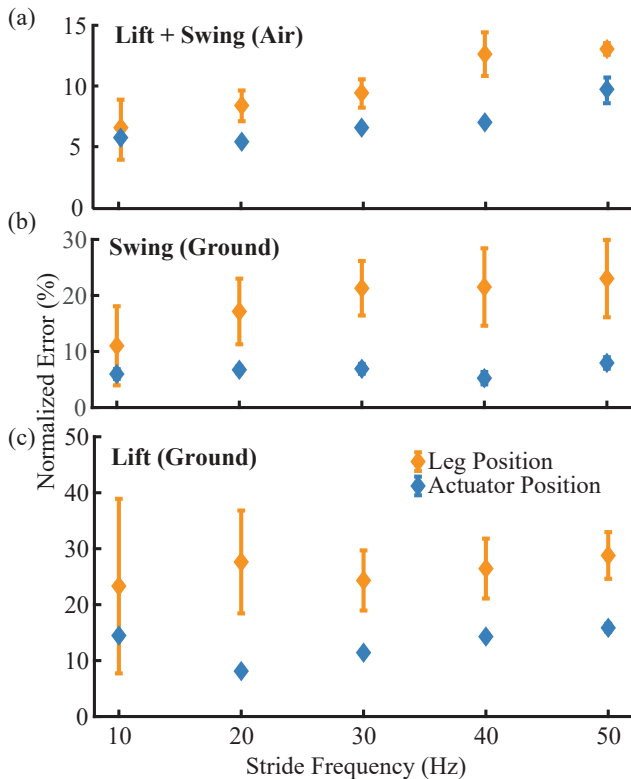


Figure 5. (a) Mean and standard deviation in normalized estimator error (\bar{E}_{est}) without ground contact in actuator position (blue, $n = 2$ transmissions) and leg position (orange, $n = 8$ transmissions) as a function of stride frequency. (b) Mean and standard deviation for normalized estimator error with ground contact in actuator position (blue, $n=1$ transmission) and leg position (orange, $n=4$ transmissions) for the swing DOF (top) and the lift DOF (bottom). All values of normalized estimation error for (a) and (b) are computed over $N = 15$ cycles.

and (2) serial compliance between the actuator and mechanical ground [48].

We find that the normalized leg position error (orange) with ground contact is higher than normalized actuator position-error (blue). The leg- x error (l_x , Fig. 5b) ranges from 11% to 24%, and leg- z error ranges (l_z , Fig. 5c) from 23% to 29%. The most likely cause of this is the serial compliance in the transmission—a common problem in flexure-based devices [39, 48]. This serial compliance alters the kinematics of the transmission by effectively adding unmodeled DOFs between the actuators and leg and changes the assumed one-to-one mapping between actuator and leg positions.

7.2. Controller

A representative trial is shown in Fig. 6a, and we quantify the normalized tracking error (\bar{E}_{cont}) for this trial as approximately 7% for both DOFs, indicating good tracking performance. Overall, we find that

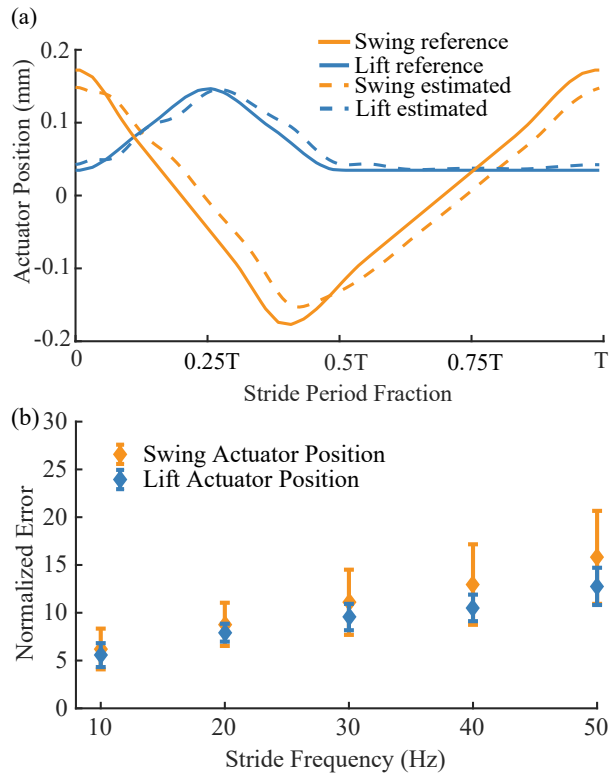


Figure 6. (a) A one-cycle comparison between the swing (orange) and lift (blue) mean experimental (dashed) and reference (solid) actuator positions for a representative trial (trot gait, $T = 1/20$, $S_1 = 60$, $S_2 = -25$). The normalized swing and lift errors are 6.96% and 7.50%, respectively. (b) Mean and standard deviation in normalized tracking error (\bar{E}_{cont}) in swing (orange, $n=8$ transmissions) and lift (blue, $n=8$ transmissions) actuator positions as a function of frequency. All values of normalized tracking error are computed across $n = 1200$ cycles and four transmissions.

normalized tracking error (Fig. 6b) for both the swing and lift DOFs is small and it monotonically increases from 6% at 10 Hz to 16% at 50 Hz. A likely reason for the increase in error as a function of stride frequency is that the high-frequency components in the heuristically designed leg trajectories become harder to track as the approach the robot’s transmission resonant frequency (between 80–100 Hz, [49]).

8. Locomotion performance

The average value for each locomotion performance metric described in Sec. 6.4 are plotted as a function of the shape control parameters (Tab. 1) at all five tested stride frequencies (10-50 Hz) in Fig. 7. We first summarize the robot’s locomotion performance for the trot gait, validate hypotheses H_1 and H_3 , and invalidate hypothesis H_2 . We then summarize performance for the pronk gait and validate hypotheses H_1 and H_4 .

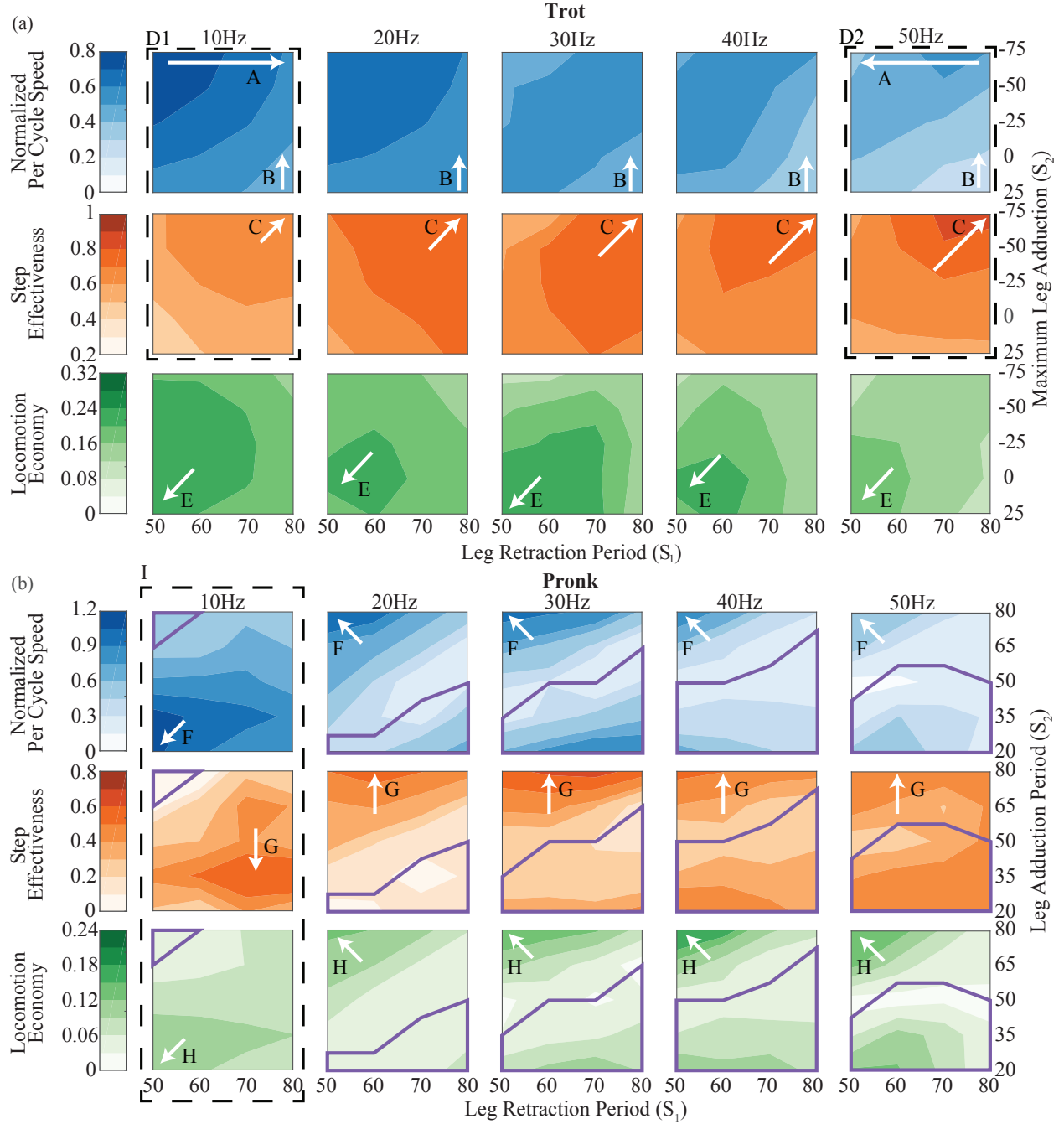


Figure 7. Contour plots depict the effect of the trajectory parameters, S_1 (x -axis) and S_2 (y -axis), on locomotion performance quantified by normalized per-cycle speed (blue), stride effectiveness (orange) and locomotion economy (green) as a function of stride frequency (10-50 Hz). (a) For the trot gait, the trajectory parameters are Leg Retraction Period (x -axis) and Maximum Leg Adduction (y -axis). (b) For the pronk gait, the same are Leg Retraction Period (x -axis) and Leg Adduction Period (y -axis). The purple polygons indicate regions where locomotion was backward. Labels A-H refer to points of specific interest and are discussed in the text in Sec. 8.

8.1. Trot Gait Performance Summary

As shown in Fig. 7a, we are able to achieve locomotion over a wide range of speeds (43-278 mm s^{-1} or 0.95-6.17 BL s^{-1} , $n = 200$ trials, $N = 2$ robots) by varying stride frequency and the shape control parameters. We also measure step effectiveness for the above gaits ranging from 0.25 to 0.91 (Fig. 7a). In addition, we

find that locomotion economy (Fig. 7a) varies nearly four-fold (0.08-0.30) and shows a strong dependence on shape control parameters both within and across frequencies. The resulting cost of transport (COT) values range from 3.33 to 13.14, and are some of the lowest measured on this platform [35, 37]. Finally, we note that cost of transport increases with frequency while maintaining a trot, supporting the hypothesis

that the preferred gait varies as a function of running speed [50]. The best and worst performing trials are visualized in supplementary video S2.

8.2. H_1 - Trot Gait

For all stride frequencies, a higher leg retraction period results in increased step effectiveness (C, Fig. 7a). Leg retraction period, however, is only positively correlated with per-cycle velocity at high stride frequencies (A, Fig. 7a). Finally, a higher leg retraction period results in lower locomotion economy at all stride frequencies (E, Fig. 7a). These trends support our initial hypothesis (H_1) that increasing leg retraction period increases step effectiveness by decreasing slipping. However, step effectiveness is only a good predictor of speed at high stride frequencies (D2, Fig. 7a), and the two are uncorrelated at low stride frequencies (D1, Fig. 7a). This is because the body dynamics (Fig. S1) have a dominating effect on speed at lower stride frequencies. These dynamics, however, are attenuated at higher stride frequencies, and, therefore, speed in those regimes is largely determined by the magnitude of foot slipping [37]. Finally, the negative correlation between locomotion economy and leg retraction period indicates that the energetic cost of tracking the high-velocity leg protraction might offset the benefit of mitigating leg slip.

8.3. H_2 and H_3 - Trot Gait

For all stride frequencies, higher maximum leg adduction results in both higher step effectiveness (C, Fig. 7a) and higher per-cycle velocity (B, Fig. 7a). These trends refute our initial hypothesis (H_2) that increasing the maximum leg adduction reduces locomotion performance in terms of speed. It is likely that higher maximum leg adduction results in increased normal and frictional support, both reducing slipping and improving forward speed.

Furthermore, increasing maximum leg adduction increases the effective leg stiffness (see Fig. S2 and Note S3) and this likely allows for greater energy storage and return, facilitating faster locomotion and supporting our initial hypothesis (H_3). However, higher maximum leg adduction results in lower locomotion economy across all stride frequencies (E, Fig. 7a). This suggests that increasing maximum leg adduction increases power consumption; however, this increase does not enable proportional gains in output mechanical power (i.e., forward speed) and results in less effective locomotion.

8.4. Pronk Gait Performance Summary

We find that modulating the timing between vertical and fore-aft leg motions enables locomotion over a wide range of speeds (-176 - 236 mm s^{-1} or -3.91 - 5.24 BL s^{-1} , $n = 200$ trials, $N = 2$ robots; blue contours in Fig. 7b) in both forward and reverse directions. The fastest trials ($\nu > 1$) are highly dynamic with long aerial and short stance phases. We also observe that step effectiveness varies from 0.01 to 0.76 (orange contours, Fig. 7b). In addition, we find that locomotion economy (green contours, Fig. 7b) varies nearly fifteen-fold (0.02-0.24). The resulting COT values (4.21 to 64.84) span the range from being among the lowest measured for this platform to some of the highest at each frequency. Finally, we note that actuator per-cycle energy consumption is independent of the stride frequency and the gait shape control parameters, and, as a consequence, the contour maps of ϵ mirror that of ν . The best and worst performing trials are visualized in supplementary video S3.

8.5. H_1 - Pronk Gait

We find that the lowest leg retraction period results in the highest per-cycle velocity (F, Fig. 7b) and locomotion economy (H, Fig. 7b) across all stride frequencies. This matches our intuition that rapid leg swing retraction during stance is key to maximizing the net forward impulse imparted to the robot. Furthermore, we do not see a clear trend in the dependence of step effectiveness on leg retraction period (G, Fig. 7b); however, we again see that step effectiveness is a good predictor of normalized per-cycle speed at higher stride frequencies. These trends refute our initial hypothesis H_1 that increasing leg retraction period reduces leg slip and therefore results in improved performance.

8.6. H_4 - Pronk Gait

A high leg adduction period and low swing retraction period results in fast forward locomotion (F, Fig. 7b), high step effectiveness (G, Fig. 7b), and high locomotion economy (H, Fig. 7b) for stride frequencies from 20–50 Hz. Similarly, a low leg adduction period and high leg retraction period results in fast backwards (enclosed by a purple polygon) locomotion and high locomotion economy. Finally, intermediate values of leg adduction (independent of leg retraction) result in ineffective locomotion. This supports our initial hypothesis (H_4) that the timing between vertical and fore-aft leg motions is crucial in determining locomotion performance and direction. In contrast, we observe a reversal in the trends described above (I, Fig. 7b) at a stride frequency of 10 Hz where the robots

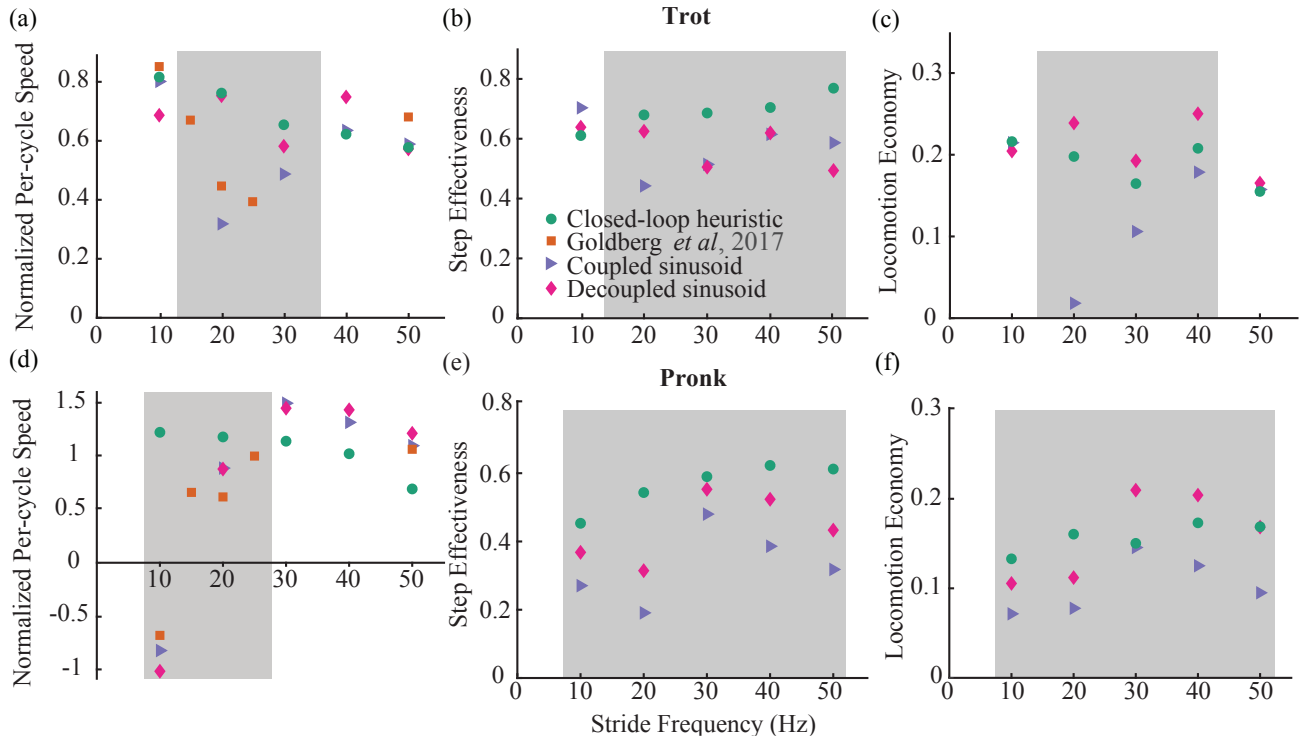


Figure 8. Plot of performance metrics – (a,d) maximum normalized per-cycle speed, (b,e) step effectiveness, and (c,f) locomotion economy – as a function of stride frequency (10-50 Hz) for the trot (top row) and prong (bottom row) gaits. We compared performance across four different types of trajectories: closed-loop heuristic (green circles, 6.3), best performing trajectories from Goldberg *et al.* (orange squares, [37]), coupled sinusoidal (blue triangles, 6.5.1), decoupled sinusoidal (magenta diamonds, 6.5.2). The gray shaded regions indicate where the closed-loop heuristic trajectories outperformed the coupled sinusoidal trajectories.

mechanical z -resonance results in long flight phases that favor a shorter leg adduction period.

9. Effective Locomotion Performance Across Dynamic Regimes

We analyze the best performing trials (Fig. 8) to test our final hypothesis (H_5) that closed-loop trajectory modulation enables high-performance locomotion across stride frequencies. Using speed as the primary metric to facilitate a comparison with previous results from [37], we define the best performing trial as the one with the highest normalized per cycle speed (ν) at each frequency for the trot and prong, respectively. However, we also plot step effectiveness (ϵ) and locomotion economy (σ) for the best performing trials to consider multi-dimensional robot performance.

For the trot gait, we find that closed-loop heuristic trajectories allow the robot to maintain high speed locomotion across all stride frequencies (Fig. 8a). This is in contrast with the open-loop results from [37] and the coupled sinusoidal trajectories (Sec. 6.5.1) where the robot suffers from poor performance in intermediate frequency regimes (15–35 Hz, supplementary video S1). However, we find that there is minimal difference in robot

speed when using either the closed-loop heuristic leg trajectories or the decoupled sinusoidal trajectories (Sec. 6.5.2). A similar trend is observed with locomotion economy (Fig. 8c); however, the closed-loop heuristic trajectories enable higher step effectiveness at all stride frequencies greater than 10 Hz (Fig. 8b). These results suggest that, while the shape of leg trajectories is important for effective locomotion using the trot gait in the body dynamics regime (15–35 Hz), the distribution of energy between the leg vertical and fore-aft motion achieved via leg shape modulation is the significant consideration at operating conditions where the dynamics are neither mechanically tuned (10 Hz) nor attenuated (40-50 Hz).

Similarly, we also find that closed-loop heuristic trajectories allow the robot to maintain speed across all stride frequencies (Fig. 8d) when using a prong gait. This is in contrast with the open-loop results from [37], the coupled sinusoidal trajectories, and the decoupled sinusoidal trajectories where the robot suffers from poor performance between 5–25 Hz (supplementary video S1). On the other hand, closed-loop heuristic trajectories enable higher step effectiveness (Fig. 8e) and locomotion economy (Fig. 8f) across all stride frequencies compared to coupled input matched open-loop trajectories. This validates hypothesis H_5 , indicating that leg trajectory modulation enables high

performance locomotion across stride frequencies.

10. Conclusion and Future Work

We have presented a computationally efficient framework for proprioceptive sensing and control of leg trajectories on a quadrupedal microrobot. We used this novel capability to explore two parametric leg trajectories designed to test a series of hypotheses that investigate the influence of leg slipping, stiffness, timing, and energy on locomotion performance. This parameter sweep resulted in an experimental performance map that allowed us to select control parameters and determine a leg trajectory that maximized performance at a desired gait and stride frequency. Using these parameters, we recovered effective performance over a wide range of stride frequencies, achieving locomotion that is robust to perturbations arising from the robot's body dynamics [51].

Specifically, for the trot gait, we demonstrated that maximizing robot speed depends on minimizing slipping at high stride frequencies and leveraging favorable at low and intermediate stride frequencies. We found that the mechanism for doing either was modulating leg trajectory shape, and consequently, input energy. In addition, we were able to increase energy storage and return by modulating leg stiffness, which resulted in faster locomotion. Furthermore, we found that leg timing determined performance for the pronk gait and allowed for rapid locomotion in the forward or backwards directions.

In the future, we aim to use this low-level controller in conjunction with trajectory optimization as in [43] to design feasible leg trajectories that optimize a given cost (e.g., speed, COT, etc.) at a particular operating condition. This can automate the challenging task of designing appropriate leg trajectories for a complex legged system and result in better locomotion performance. We can also use this controller in conjunction with computationally efficient whole-body locomotion controllers as in [32, 33] and ensure accurate tracking of the leg trajectories during a variety of locomotion modalities including swimming [52] or climbing [53] with HAMR. Finally, we can use the results from this work to inform future mechanical design decisions. For example, increasing the transmission resonant frequencies [49] can increase control authority and enable improved leg trajectory control at the higher stride frequencies (40–50 Hz) tested in this work. Ultimately, our results suggest that HAMR could be a strong candidate platform for systematically testing hypotheses about biological locomotion such as the effect of varying leg trajectories on locomotion [54].

Acknowledgements

Thank you to all members of the Harvard Micro-robotics and Agile Robotics Laboratories for invaluable discussions. This work is partially funded by the Wyss Institute for Biologically Inspired Engineering. In addition, the prototypes were enabled by equipment supported by the ARO DURIP program (award #W911NF-13-1-0311).

References

- [1] S. M. Manton, *The Arthropoda: habits, functional morphology and evolution*. Oxford University Press, 1977, no. QL434. M36 1977.
- [2] S. Gatesy and A. Biewener, "Bipedal locomotion: effects of speed, size and limb posture in birds and humans," *Journal of Zoology*, vol. 224, no. 1, pp. 127–147, 1991.
- [3] H. Geyer, A. Seyfarth, and R. Blickhan, "Compliant leg behaviour explains basic dynamics of walking and running," *Proceedings of the Royal Society B: Biological Sciences*, vol. 273, no. 1603, pp. 2861–2867, 2006.
- [4] M. Kenning, C. H. Müller, and A. Sombke, "The ultimate legs of chilopoda (myriapoda): a review on their morphological disparity and functional variability," *PeerJ*, vol. 5, p. e4023, 2017.
- [5] M. A. Daley and A. A. Biewener, "Muscle force-length dynamics during level versus incline locomotion: a comparison of in vivo performance of two guinea fowl ankle extensors," *Journal of Experimental Biology*, vol. 206, no. 17, pp. 2941–2958, 2003.
- [6] A. V. Birn-Jeffery, C. M. Hubicki, Y. Blum, D. Renjewski, J. W. Hurst, and M. A. Daley, "Don't break a leg: running birds from quail to ostrich prioritise leg safety and economy on uneven terrain," *Journal of Experimental Biology*, vol. 217, no. 21, pp. 3786–3796, 2014.
- [7] T. A. McMahon, "The role of compliance in mammalian running gaits," *Journal of Experimental Biology*, vol. 115, no. 1, pp. 263–282, 1985.
- [8] M. A. Daley and A. A. Biewener, "Running over rough terrain reveals limb control for intrinsic stability," *Proceedings of the National Academy of Sciences*, vol. 103, no. 42, pp. 15 681–15 686, 2006.
- [9] S. Wilshin, M. A. Reeve, G. C. Haynes, S. Revzen, D. E. Koditschek, and A. J. Spence, "Longitudinal quasi-static stability predicts changes in dog gait on rough terrain," *Journal of Experimental Biology*, pp. jeb-149 112, 2017.
- [10] M. H. Dickinson, C. T. Farley, R. J. Full, M. Koehl, R. Kram, and S. Lehman, "How animals move: an integrative view," *science*, vol. 288, no. 5463, pp. 100–106, 2000.
- [11] S. N. Gorb, "Design of the predatory legs of water bugs (hemiptera: Nepidae, naucoridae, notonectidae, gerridae)," *Journal of morphology*, vol. 223, no. 3, pp. 289–302, 1995.
- [12] K. Jayaram, J.-M. Mongeau, A. Mohapatra, P. Birkmeyer, R. S. Fearing, and R. J. Full, "Transition by head-on collision: mechanically mediated manoeuvres in cockroaches and small robots," *Journal of The Royal Society Interface*, vol. 15, no. 139, p. 20170664, 2018.
- [13] E. Yang, J. H. Son, S.-i. Lee, P. G. Jablonski, and H.-Y. Kim, "Water striders adjust leg movement speed to optimize takeoff velocity for their morphology," *Nature Communications*, vol. 7, pp. 13 698 EP –, 12 2016. [Online]. Available: <https://doi.org/10.1038/ncomms13698>

- [14] K. Jayaram and R. J. Full, “Cockroaches traverse crevices, crawl rapidly in confined spaces, and inspire a soft, legged robot,” *Proceedings of the National Academy of Sciences*, vol. 113, no. 8, pp. E950–E957, 2016.
- [15] Y. Sakagami, R. Watanabe, C. Aoyama, S. Matsunaga, N. Higaki, and K. Fujimura, “The intelligent asimo: System overview and integration,” in *Intelligent Robots and Systems, 2002. IEEE/RSJ International Conference on*, vol. 3. IEEE, 2002, pp. 2478–2483.
- [16] C. Hubicki, J. Grimes, M. Jones, D. Renjewski, A. Spröwitz, A. Abate, and J. Hurst, “Atrias: Design and validation of a tether-free 3d-capable spring-mass bipedal robot,” *The International Journal of Robotics Research*, vol. 35, no. 12, pp. 1497–1521, 2016.
- [17] M. Raibert, K. Blankespoor, G. Nelson, and R. Playter, “Bigdog, the rough-terrain quadruped robot,” *IFAC Proceedings Volumes*, vol. 41, no. 2, pp. 10822–10825, 2008.
- [18] S. Seok, A. Wang, M. Y. M. Chuah, D. J. Hyun, J. Lee, D. M. Otten, J. H. Lang, and S. Kim, “Design principles for energy-efficient legged locomotion and implementation on the mit cheetah robot,” *IEEE/ASME Transactions on Mechatronics*, vol. 20, no. 3, pp. 1117–1129, 2015.
- [19] C. Semini, V. Barasuol, J. Goldsmith, M. Frigerio, M. Focchi, Y. Gao, and D. G. Caldwell, “Design of the hydraulically-actuated, torque-controlled quadruped robot hyq2max,” *IEEE/ASME Transactions on Mechatronics*, vol. PP, no. 99, pp. 1–1, 2016.
- [20] M. Hutter, C. Gehring, M. Bloesch, M. A. Hoepffinger, C. D. Remy, and R. Siegwart, “Starleth: A compliant quadrupedal robot for fast, efficient, and versatile locomotion,” in *Adaptive Mobile Robotics*. World Scientific, 2012, pp. 483–490.
- [21] S. Kuindersma, R. Deits, M. Fallon, A. Valenzuela, H. Dai, F. Permenter, T. Koolen, P. Marion, and R. Tedrake, “Optimization-based locomotion planning, estimation, and control design for the atlas humanoid robot,” *Autonomous Robots*, vol. 40, no. 3, pp. 429–455, 2016.
- [22] U. Saranli, M. Buehler, and D. E. Koditschek, “Rhcx: A simple and highly mobile hexapod robot,” *The International Journal of Robotics Research*, vol. 20, no. 7, pp. 616–631, 2001.
- [23] P. Birkmeyer, K. Peterson, and R. S. Fearing, “Dash: A dynamic 16g hexapedal robot,” in *2009 IEEE/RSJ International Conference on Intelligent Robots and Systems*, Oct 2009, pp. 2683–2689.
- [24] R. S. Pierre and S. Bergbreiter, “Gait exploration of sub-2 g robots using magnetic actuation.” *IEEE Robotics and Automation Letters*, vol. 2, no. 1, pp. 34–40, 2017.
- [25] A. G. Dharmawan, H. H. Hariri, G. S. Soh, S. Foong, and K. L. Wood, “Design, analysis, and characterization of a two-legged miniature robot with piezoelectric-driven four-bar linkage,” *Journal of Mechanisms and Robotics*, vol. 10, no. 2, p. 021003, 2018.
- [26] S. A. Bailey, J. G. Cham, M. R. Cutkosky, and R. J. Full, “Comparing the locomotion dynamics of the cockroach and a shape deposition manufactured biomimetic hexapod,” in *Experimental Robotics VII*. Berlin, Heidelberg: Springer Berlin Heidelberg, 2001, pp. 239–248.
- [27] S. Kim, J. E. Clark, and M. R. Cutkosky, “isprawl: Design and tuning for high-speed autonomous open-loop running,” *The International Journal of Robotics Research*, vol. 25, no. 9, pp. 903–912, 2006.
- [28] D. W. Haldane and R. S. Fearing, “Running beyond the bio-inspired regime,” in *2015 IEEE International Conference on Robotics and Automation (ICRA)*, May 2015, pp. 4539–4546.
- [29] D. W. Haldane, M. M. Plecnik, J. K. Yim, and R. S. Fearing, “Robotic vertical jumping agility via series-elastic power modulation,” *Science Robotics*, vol. 1, no. 1, 2016.
- [30] P. Birkmeyer, A. G. Gillies, and R. S. Fearing, “Clash: Climbing vertical loose cloth,” in *2011 IEEE/RSJ International Conference on Intelligent Robots and Systems*, Sept 2011, pp. 5087–5093.
- [31] —, “Dynamic climbing of near-vertical smooth surfaces,” in *2012 IEEE/RSJ International Conference on Intelligent Robots and Systems*, Oct 2012, pp. 286–292.
- [32] K. Karydis, I. Poulakakis, J. Sun, and H. G. Tanner, “Probabilistically valid stochastic extensions of deterministic models for systems with uncertainty,” *The International Journal of Robotics Research*, vol. 34, no. 10, pp. 1278–1295, 2015.
- [33] A. Nagabandi, G. Yang, T. Asmar, R. Pandya, G. Kahn, S. Levine, and R. S. Fearing, “Learning image-conditioned dynamics models for control of underactuated legged millirobots,” in *2018 IEEE/RSJ International Conference on Intelligent Robots and Systems (IROS)*. IEEE, 2018, pp. 4606–4613.
- [34] A. T. Baisch, O. Ozcan, B. Goldberg, D. Ithier, and R. J. Wood, “High speed locomotion for a quadrupedal microrobot,” *The International Journal of Robotics Research*, vol. 33, no. 8, pp. 1063–1082, 2014.
- [35] B. Goldberg, N. Doshi, K. Jayaram, J. S. Koh, and R. J. Wood, “A high speed motion capture method and performance metrics for studying gaits on an insect-scale legged robot,” in *2017 IEEE/RSJ International Conference on Intelligent Robots and Systems (IROS)*, Sept 2017, pp. 3964–3970.
- [36] B. Goldberg, N. Doshi, and R. J. Wood, “High speed trajectory control using an experimental maneuverability model for an insect-scale legged robot,” in *2017 IEEE International Conference on Robotics and Automation (ICRA)*, May 2017, pp. 3538–3545.
- [37] B. Goldberg, N. Doshi, K. Jayaram, and R. J. Wood, “Gait studies for a quadrupedal microrobot reveal contrasting running templates in two frequency regimes,” *Bioinspiration and Biomimetics*, vol. 12, no. 4, p. 046005, 2017.
- [38] K. Jayaram, N. Jafferis, N. Doshi, B. Goldberg, and R. J. Wood, “Concomitant sensing and actuation for piezoelectric microrobots,” 2018, in review.
- [39] N. Doshi, B. Goldberg, R. Sahai, N. Jafferis, D. Aukes, and R. J. Wood, “Model driven design for flexure-based microrobots,” in *2015 IEEE/RSJ International Conference on Intelligent Robots and Systems (IROS)*, Sept 2015, pp. 4119–4126.
- [40] N. T. Jafferis, M. J. Smith, and R. J. Wood, “Design and manufacturing rules for maximizing the performance of polycrystalline piezoelectric bending actuators,” *Smart Materials and Structures*, vol. 24, no. 6, p. 065023, 2015. [Online]. Available: <http://stacks.iop.org/0964-1726/24/i=6/a=065023>
- [41] M. Karpelson, G.-Y. Wei, and R. J. Wood, “Driving high voltage piezoelectric actuators in microrobotic applications,” *Sensors and Actuators A: Physical*, vol. 176, pp. 78 – 89, 2012.
- [42] P. Varin and S. Kuindersma, “A constrained kalman filter for rigid body systems with frictional contact,” in *International Workshop on the Algorithmic Foundations of Robotics (WAFR)*, 2018.
- [43] N. Doshi, K. Jayaram, B. Goldberg, Z. Manchester, R. J. Wood, and S. Kuindersma, “Contact-implicit optimization of locomotion trajectories for a quadrupedal microrobot,” in *2018 Robotics Science and Systems*, 2018, in review.
- [44] L. Ljung, “System identification,” in *Signal analysis and prediction*. Springer, 1998, pp. 163–173.

- [45] W. F. Arnold and A. J. Laub, "Generalized eigenproblem algorithms and software for algebraic riccati equations," *Proceedings of the IEEE*, vol. 72, no. 12, pp. 1746–1754, Dec 1984.
- [46] G. A. Cavagna, N. C. Heglund, and C. R. Taylor, "Mechanical work in terrestrial locomotion: two basic mechanisms for minimizing energy expenditure," *American Journal of Physiology-Regulatory, Integrative and Comparative Physiology*, vol. 233, no. 5, pp. R243–R261, 1977.
- [47] R. M. Alexander, *Principles of animal locomotion*. Princeton University Press, 2003.
- [48] O. Ozcan, A. T. Baisch, D. Ithier, and R. J. Wood, "Powertrain selection for a biologically-inspired miniature quadruped robot," in *Robotics and Automation (ICRA), 2014 IEEE International Conference on*. IEEE, 2014, pp. 2398–2405.
- [49] N. Doshi, K. Jayaram, B. Goldberg, and R. J. Wood, "Phase control for a legged microrobot operating at resonance," in *2017 IEEE International Conference on Robotics and Automation (ICRA)*, May 2017, pp. 5969–5975.
- [50] M. Hildebrand, "Symmetrical gaits of horses," *Science*, vol. 150, no. 3697, pp. 701–708, 1965.
- [51] E. Jen, *Robust design: a repertoire of biological, ecological, and engineering case studies*. Oxford University Press, 2005.
- [52] Y. Chen, N. Doshi, B. Goldberg, H. Wang, and R. J. Wood, "Controllable water surface to underwater transition through electrowetting in a hybrid terrestrial-aquatic microrobot," *Nature Communications*, vol. 9, no. 1, p. 2495, June 2018. [Online]. Available: <https://doi.org/10.1038/s41467-018-04855-9>
- [53] S. D. de Rivaz, B. Goldberg, N. Doshi, K. Jayaram, J. Zhou, and R. J. Wood, "Inverted and vertical climbing of a quadrupedal microrobot using electroadhesion," *Science Robotics*, vol. 3, no. 25, 2018. [Online]. Available: <http://robotics.sciencemag.org/content/3/25/eaau3038>
- [54] H. Cruse, V. Dürr, M. Schilling, and J. Schmitz, "Principles of insect locomotion," in *Spatial temporal patterns for action-oriented perception in roving robots*. Springer, 2009, pp. 43–96.